The Astrophysical Journal, 908:166 (14pp), 2021 February 20 https://doi.org/10.3847/1538-4357/abd4e2

Far-Infrared Line Diagnostics: Improving N/O Abundance Estimates for Dusty Galaxies

B. Peng[1], C. Lamarche[2], G. J. Stacey[1], T. Nikola[3], A. Vishwas[3], C. Ferkinhoff[4], C. Rooney[1], C. Ball[1], D. Brisbin[5], J. Higdon[6], and S. J. U. Higdon[6]
[1] Department of Astronomy, Cornell University, Ithaca, NY 14853, USA; bp392@cornell.edu
[2] Department of Physics and Astronomy, University of Toledo, 2801 West Bancroft Street, Toledo, OH 43606, USA
[3] Cornell Center for Astrophysics and Planetary Science, Cornell University, Ithaca, NY 14853, USA
[4] Department of Physics, Winona State University, Winona, MN 55987, USA
[5] Joint ALMA Observatory, Alonso de Cordova 3107, Vitacura, Santiago, Chile
[6] Department of Physics, Georgia Southern University, Statesboro, GA 30460, USA
Received 2020 September 4; revised 2020 December 15; accepted 2020 December 16; published 2021 February 22

Abstract

The nitrogen-to-oxygen (N/O) abundance ratio is an important diagnostic of galaxy evolution because the ratio is closely tied to the growth of metallicity and the star formation history in galaxies. Estimates for the N/O are traditionally made with optical lines that could suffer from extinction and excitation effects, so the N/O is arguably measured better through far-infrared (far-IR) fine-structure lines. Here we show that the [N III]57 μm/[O III]52 μm line ratio, denoted N3O3, is a physically robust probe of N/O. This parameter is insensitive to gas temperature and only weakly dependent on electron density. Although it has a dependence on the hardness of the ionizing radiation field, we show that it is well corrected when the [Ne III]15.5 μm/[Ne II]12.8 μm line ratio is included. We verify the method, and characterize its intrinsic uncertainties by comparing the results to photoionization models. We then apply our method to a sample of nearby galaxies using new observations obtained with SOFIA/FIFI-LS in combination with available Herschel/PACS data, and the results are compared with optical N/O estimates. We find evidence for a systematic offset between the far-IR and optically derived N/O. We argue that the likely reason is that our far-IR method is biased toward younger and denser H II regions, while the optical methods are biased toward older H II regions as well as diffuse ionized gas. This work provides a local template for studies of the abundance of interstellar medium in the early Universe.

Unified Astronomy Thesaurus concepts: Galaxy evolution (594); Chemical abundances (224); Abundance ratios (11); Far infrared astronomy (529)

Supporting material: figure set

1. Introduction

Because metal elements heavier than lithium are formed in stars, their abundance is a key parameter for galaxy evolution studies. However, the absolute abundances are particularly difficult to measure, while the relative abundance of nitrogen to oxygen (N/O) is more reliably obtained. The N/O has been shown to be strongly correlated with the absolute metallicity (O/H) and is a probe of star formation history. In particular, the N/O follows a segmented relation to metallicity, such that at low metallicities, N/O stays nearly constant, but when $\log(\mathrm{O/H}) > -3.7$, it starts to increase with metallicity. This trend is seen in H II regions of nearby galaxies (e.g., Garnett 1990; Vila-Costas & Edmunds 1993; van Zee et al. 1998; Pilyugin et al. 2010), large surveys of galaxies (Pérez-Montero et al. 2013), and spatially resolved integral field unit (IFU) observation of galaxies (Pérez-Montero et al. 2016; Belfiore et al. 2017). This N/O–metallicity relation does not appear to evolve from $z = 0$ up to $z = 0.4$, but the N/O does appear to grow toward lower redshift, accompanied by an increase in metallicity (Pérez-Montero et al. 2013). The segmented relationship is thought to result from there being two origins of nitrogen: the primary production in the supernova events by massive stars, and the secondary production in mostly intermediate-mass stars (Edmunds & Pagel 1978; Henry et al. 2000; Pilyugin et al. 2003). When a galaxy is young and the gas is pristine, the primary nitrogen and oxygen dominate the chemical reservoir and maintain a nearly constant N/O; while later, the secondary nitrogen is produced and enters the interstellar medium (ISM) at a higher rate than oxygen does in the primary production, thereby increasing the N/O. The dual origins of nitrogen link the N/O to the star formation history of galaxies. Edmunds & Pagel (1978) first proposed to use the N/O as an indicator of the "age" of a galaxy, by which we mean the time since the last major star formation event that built up most of the stars in the galaxy. This idea is supported by various observations and models including Unger et al. (2000), Pilyugin et al. (2003), Mollá et al. (2006), Vincenzo et al. (2016), Vangioni et al. (2018), and others. In addition to age, N/O can help study other aspects of galaxy evolution such as the burstiness of star formation (Garnett 1990; Coziol et al. 1999; Mouhcine & Contini 2002) and the effect of feedback on chemical evolution (Vincenzo et al. 2016; Contini 2017).

The N/O is also vitally important for studying metallicity. Directly or indirectly, N/O is integrated into several commonly used metallicity indices. These include the N2 parameter ([N II]/Hα; Denicoló et al. 2002), the N2O2 index ([N II]λ6584/[O II]λ3727; Kewley & Dopita 2002), the O3N2 parameter ([N II]λ6584/[O III]λ5007; Pettini & Pagel 2004), and the [O III]52 to [N III]57 μm ratio (Unger et al. 2000; Pereira-Santaella et al. 2017). These methods measure either the N/O or the nitrogen abundance in the first place, then extrapolate to the oxygen abundance by assuming certain N/O to metallicity relations, regardless of the large scatter in this relationship. Moreover, in most of the photoionization model studies of metallicity, the nitrogen abundance is input as a parameter dependent on the oxygen abundance by adopting a N/O–metallicity relation. The use of a N/O–metallicity relation in the cases above could introduce appreciable uncertainty in these metallicity diagnostics, and systematically undermines the robustness of N/O–metallicity relation calibrated through optical strong line methods (Pérez-Montero & Contini 2009; Stasinska 2019; Schaefer et al. 2020). Therefore it is crucial to obtain precise N/O measurements to better constrain gas-phase metallicities and to understand the star formation in galaxies.

Most previous studies of N/O diagnostics focused on the optical strong line ratios, and are based on an assumption that the line flux ratio traces the fraction of the amount of emitting ions, which should be equal to the N/O abundance ratio. One widely used method is the N2O2 parameter (Kewley & Dopita 2002), deemed to measure the N^+/O^+ ion ratio. The O3N2 parameter (Pettini & Pagel 2004) follows a similar logic, but relates to the O^{++} ion. The lines from another primary element, sulfur, can be used instead of oxygen lines, as in the N2S2 parameter ([N II] λ6584/[S II]λ6717+6731; Viironen et al. 2007). These methods are subject to the common drawbacks of optical lines: optical lines often suffer from dust extinction, especially in dusty galaxies with a high star formation rate (SFR) such as luminous infrared galaxies (LIRGs); forbidden line fluxes depend exponentially on the electron temperature, which in H II regions is comparable to the optical-line excitation potentials. According to Pérez-Montero & Contini (2009), N2O2 and N2S2 have a dispersion of 0.24 and 0.31 dex, respectively. To cope with these issues, corrections for temperature and density are usually introduced (see Pagel et al. 1992; Pilyugin et al. 2010), although such corrections introduce more statistical errors that could worsen the overall uncertainties.

The far-IR fine-structure lines have significant advantages over optical lines in probing the ISM physical properties. At wavelengths much greater than the size scales of interstellar dust, they are not greatly affected by dust extinction. The lines arise from levels only a few hundred K above the ground state, so that they are insensitive to the gas temperature in H II regions. Furthermore, the line emission is typically optically thin, so radiative transfer effects are minor. Therefore the far-IR lines of O^{++}, N^+, and N^{++} ions serve as reliable proxies to diagnose the N/O. Far-IR diagnostics of N/O were first introduced by Lester et al. (1983), who used the [N III]57 μm-to-[O III]52 μm line ratio, and applied it to a large sample of H II regions in the Milky Way (Lester et al. 1987). This diagnostic was later calibrated in Rubin et al. (1988) using the photoionization model grids in Rubin (1985) to account for the different O^{++} and N^{++} volumes in varied radiation fields. This line ratio was explored in the extragalactic context first with ISO observations (Unger et al. 2000), then with Herschel/PACS (Nagao et al. 2011; Pereira-Santaella et al. 2017) as a probe of metallicity. Unger et al. (2000) made a correction for ionization based on the [N II]122 μm-to-[N III]57 μm line ratio, but the other papers neglected the effect of radiation hardness, which has an important effect on the [N III]-to-[O III]52 line ratio. Also based on the oxygen and nitrogen far-IR line ratio, [O III]88 μm/[N II]122 μm is used to estimate metallicity in Rigopoulou et al. (2018), although it can be argued that the 88-to-122 um ratio is a better indicator of radiation field hardness (Ferkinhoff et al. 2011). In this paper the [N III]-to-[O III]52 line ratio is revisited as a diagnostic of N/O with the effect of the radiation field hardness more carefully considered, and the line ratio probes are calibrated by more recent photoionization model grids that explore a larger parameter space than were given in Rubin (1985).

Table 1
Characteristic of the Mid-IR and Far-IR Lines Used for N/O Diagnostic

Line	E (eV)	λ (μm)	$n_{\rm crit}$ (cm^{-3})
[N III]$^2P_{3/2} - {}^2P_{1/2}$	29.60	57.32	2.1×10^3
[O III]$^3P_2 - {}^3P_1$	35.12	51.81	3.6×10^3
[O III]$^3P_1 - {}^3P_0$	35.12	88.36	510
[Ne II]$^2P_{1/2} - {}^2P_{3/2}$	21.56	12.81	7.0×10^5
[Ne III]$^3P_1 - {}^3P_2$	40.96	15.56	2.7×10^5

Note. The columns are the formation potential of the line-emitting species, wavelength, and critical electron density of the spectral line. The data are taken from Stacey (2011) and Fernández-Ontiveros et al. (2016).

This paper is structured as follows: in Section 2, the strong line ratio N3O3 parameter and the density-corrected N3O3$_{n_e}$ parameter are introduced as first-order N/O diagnostics; in Section 3, the neon-line ratio is introduced to correct for radiation field hardness. We then use the photoionization models from the BOND and CALIFA projects to calibrate the relationship between the N3O3 parameter and the [Ne III] 15.5 μm-to-[Ne II]12.8 μm line ratio. Section 4 describes the galaxy sample and the reduction of SOFIA/FIFI-LS data to which the N3O3 diagnostic is applied. The results are then compared with the N/O reported in the literature. In Section 5 we summarize the main results, and conclude the paper by highlighting the prospects of using the N3O3 parameter for the study of chemical abundances and galaxy evolution in high-redshift galaxies.

2. The N3O3 Strong Line Method

2.1. The N3O3 Parameter

The [N III] 57 μm and [O III] 52 μm lines arise from the ground-state term of the N^{++} and O^{++} fine-structure configurations. Their emitting levels are collisionally excited by electrons in H II regions so that the line ratio is affected by the H II region physical properties and ionization structure in the following way:

$$\frac{F_{\rm [N\,III]}}{F_{\rm [O\,III]52}} \sim \frac{n({\rm N})}{n({\rm O})}\,\frac{{\rm N}^{++}/{\rm N}}{{\rm O}^{++}/{\rm O}}\,\frac{\varepsilon_{\rm [N\,III]}}{\varepsilon_{\rm [O\,III]52}}. \quad (1)$$

The first term on the right-hand side of the equation is the gas-phase N/O abundance ratio, the second term is the ratio of the fractions of N and O that are doubly ionized, and the last term is the ratio of emissivity, defined here as the power emitted in the line per ion. The emissivity is primarily a function of electron density and is more weakly dependent on electron temperature. The line emission is assumed to be optically thin.

The [N III]-to-[O III]52 line ratio is a good tracer for the N/O abundance ratio for several reasons. First, the energies required to produce both ions are very similar (Table 1), so that the N^{++} and O^{++} ions occupy very similar regions in the ISM, typically H II regions of young stars or the ionized regions surrounding active galactic nuclei (AGNs). Note that their formation potentials are just above that of helium (24.6 eV), which means that they share nearly the same volume as He^+ (Lester et al. 1983), the ion that dominates the ionization structure in the H II regions with hard radiation fields. Second, their critical densities are very similar, so that the [N III]-to-[O III] 52 μm emissivity ratio changes only by a factor of 5 from the low- to high-density limit. This is much smaller than the variation when the [O III] 88 μm line is used. Thus in Equation (1), the ionization and emissivity ratios nearly cancel out, so that the [N III]/[O III]52 line ratio is a good first-order proxy for the N/O abundance ratio. Furthermore, on large scales in galaxies, this doubly ionized line flux probe can be interpreted as arising primarily from a few H II regions with high excitation. This is different from lower ionization state lines, which come from a much larger collection of H II region excitation environments (e.g., the diffuse ionized ISM; see Díaz-Santos et al. 2017), and thus are more difficult to interpret.

Our first estimate of the N/O abundance ratio uses only the [N III]-to-[O III]52 line flux ratio:

$$\mathrm{N/O} \sim N3O3 = \frac{F_{[\mathrm{N\,III}]}}{F_{[\mathrm{O\,III}]52}} \times 0.400. \quad (2)$$

The index is called the N3O3 parameter for clarity. The numerical factor is what one obtains in the low-density limit ($n_e \ll n_{\rm crit}$) for Equation (1). For extragalactic work, this is a good approximation because electron densities in starburst galaxies are usually of an order $10^2\,\mathrm{cm}^{-3}$ (Inami et al. 2013), whereas $n_{\rm crit}$ of both lines is above $2 \times 10^3\,\mathrm{cm}^{-3}$. We have also assumed an electron temperature of $T_e = 10^4$ K, which is typical for H II regions. The exact value chosen has only a small effect on far-IR lines. A more detailed description of the parameters and details of the calculation can be found in Appendix A.2.

This method is advantageous in theoretical and practical aspects. It is based on simple arguments and is more physically robust than other N/O diagnostics, especially those involving the O^{++}-to-N^{+} ion ratio, because these ions occupy different ionization zones. It also benefits from the weaker dependence on temperature of far-IR lines over optical methods. The simplicity of using only two lines lends great applicability when studying high-redshift galaxies, where observations are often difficult or impossible due to telluric absorption, and data are therefore sparse. An additional benefit is that as one of the brightest spectral lines from star-forming galaxies, the [O III] 52 μm line encodes additional scientific value that is linked to star formation rates, and that when combined with the equally bright [O III] 88 μm line, the line pair constrains electron density and gas mass.

2.2. Density Correction of the N3O3 Parameter

Although the low-density limit works well in most cases and the simplicity of using only two lines is attractive, it is desirable to correct for the electron density dependence when the density can be estimated, for example, by the [O III]52/[O III]88 or the [N II]122/[N II]205. Therefore we also provide here a more precise diagnostic tool that is corrected for electron density and temperature. The index is denoted $\mathrm{N3O3}_{n_e}$ and is defined as

$$\mathrm{N/O} \sim N3O3_{n_e} = N3O3 \times \frac{1 + 0.691 n_e/T_e^{1/2} + 0.0966 n_e^2/T_e}{1 + 0.377 n_e/T_e^{1/2} + 0.0205 n_e^2/T_e}, \quad (3)$$

where n_e is the electron density value in units of cm^{-3} and the electron temperature T_e is in Kelvin. The correction factor starts to have a non-negligible effect at $n_e/T_e^{1/2} > 1$, and rises until the value $\sim$4.7 at the high-density end.

Clearly, the densities derived from [O III]52/88 are the best because it reuses one of the same lines as in N3O3, thereby measuring densities in the same regions. For convenience, we also provide an expression of $\mathrm{N3O3}_{n_e}$ that uses the [O III]52/88:

$$N3O3_{n_e} = N3O3 \times 6.82 \frac{R_{52/88}(R_{52/88} + 1.01)}{2.13 + 6.26 R_{52/88} + R_{52/88}^2}, \quad (4)$$

in which $R_{52/88} = \frac{F_{[\mathrm{O\,III}]52}}{F_{[\mathrm{O\,III}]88}}$ is the [O III] line flux ratio. The detailed derivation of N3O3 and $\mathrm{N3O3}_{n_e}$ as well as the parameters used for collisional excitation calculation are given in Appendix A.

3. Photoionization Model Calibration

3.1. [Ne III]/[Ne II] as a Radiation Hardness Tracer

As stated in the previous section, one of the main benefits of using [O III] and [N III] is the nearly cospatial nature of N^{++} and O^{++} ions in H II regions. In actuality, however, the O^{++} volume is usually smaller than the N^{++} volume: the volumes are only closely matched when the radiation field is hard enough such that the helium Strömgren sphere fills the whole H II region. Only in this case can the line ratio trace the abundance ratio at high accuracy without corrections for ionization structure. Furthermore, if the radiation field is too hard, our N3O3 diagnositic would fail as N^{++} becomes ionized into N^{+++} and the [N III] flux would decrease. Therefore an indicator for the radiation hardness is essential for calibrating the N3O3 diagnostic to higher precision.

We use the [Ne III] 15.5 μm-to-[Ne II] 12.8 μm line ratio as a tracer for the radiation hardness. Because their ionization potentials are 40.96 eV and 21.56 eV (Table 1), with one higher and the other lower than that of helium, the Ne^{++}-to-Ne^{+} ion ratio closely follows the fraction of volume inside and outside the helium Strömgren sphere in H II region. In addition, the critical densities of both lines are $\sim 10^5\,\mathrm{cm}^{-3}$, much higher than the typical densities in H II regions, so that their emissivity ratio is almost density invariant. This is a major advantage over the [N III]/[N II], which is another commonly used hardness tracer (see Unger et al. 2000): because the [N II] lines have relatively low critical densities ($\leqslant 200\,\mathrm{cm}^{-3}$), the line emissivity ratio is much more sensitive to the electron density at $\sim 10^2\,\mathrm{cm}^{-3}$ values. Furthermore, because the energy to ionize the third electron off from neon is 63.45 eV, higher than that energy for nitrogen (47.4 eV) or oxygen (54.9 eV), so that the neon-line ratio can still function as a hardness tracer in the environments where N^{++} ions are further ionized and the [N III]/[N II] ratio would fail.

Other factors that favor the [Ne III]15/[Ne II]12 ratio as a radiation hardness tracer include that the emitting levels are roughly 1000 K above ground so that they have reduced sensitivity to the gas temperature in H II regions compared with optical lines; they lie in the mid-IR range so that they are affected less by extinction, and they lie close in wavelength so that the differential extinction correction is small; ample data are available from mid-IR observatories (Spitzer, ISO, etc.), and both neon lines are often strong in star-forming galaxies. One caveat for the [Ne III] line is the possible contamination from AGN, however. Although it is not a concern for nearby galaxies, as spectral classification can identify AGNs, and spatial resolution is often sufficient to separate active nuclei from star-forming regions, AGN contamination might undermine its application to high-redshift objects. Fortunately, the nearby [Ne V] 14.3 μm line is only bright from AGN on galactic scales and there is a strong correlation between the [Ne III] lines and the [Ne V] line emission in nearby AGN-dominated systems, so that the fraction of the [Ne III] line that arises from the AGN is well determined by measuring the [Ne V] line (Gorjian et al. 2007).

3.2. Introduction of Photoionization Models

In order to validate the N3O3 parameter and correct it for ionization hardness with the neon-line ratio, we compare our results against photoionization models that account for different stellar populations and include detailed physical calculations on ionization structure and radiative transfer. These models can be used to study the uncertainty of this diagnostic as well because they cover a large volume in the parameter space, representative of the diversity of galaxies.

The grids of photoionization models used in this paper are drawn from the CALIFA (Cid Fernandes et al. 2014) and BOND projecta (Vale Asari et al. 2016). These models are run and hosted by the Mexican Million Models Database (3MDB; Morisset et al. 2015), available for public use.[7] All the models result from running Cloudy photoionization code v17.01 (Ferland et al. 2017) through pyCloudy (Morisset 2013).

The CALIFA Project is a grid of photoionization models that feature a broad diversity in input stellar populations, with ages ranging from 1 Myr to 14 Gyr. The N/O abundance ratio is an independent parameter in the input configuration, spanning from log N/O = −1.36 to −0.36 in five steps. These photoionization models were initially run to analyze IFU observations in the CALIFA survey (Sánchez et al. 2012).

BOND is a grid of models that also does not assume an N/O–O/H relation, and that covers a broad range in abundance of the two elements as well as radiation field strength. These models only use a fixed density of 100 $\mathrm{cm^{-3}}$ in either a filled sphere or a thin-shell geometry. The input starburst ages are 1, 2, 3, 4, 5 and 6 Myr. The spectral energy distribution (SED) of the ionizing radiation is obtained from stellar population synthesis models accounting for the appropriate metallicity.

It is essential to use both the BOND and CALIFA models because the former are run on electron density 100 $\mathrm{cm^{-3}}$ and the latter use 10 $\mathrm{cm^{-3}}$. They complement each other on electron density, which is the parameter that has the largest effect on far-IR fine-structure line emissivity. Our calibration of the N3O3 parameter below justifies the need to combine the two grids, and the usefulness of the density-corrected $\mathrm{N3O3}_{n_e}$ parameter.

Because BOND and CALIFA cover slightly different regions in the parameter space, only a subset of parameters common for both models is used for consistency. The selections of parameters are as follows:

1. Only a filled sphere geometry is used for both grids, corresponding to geometric fraction = 0.03, meaning that the inner radius is 3% of the Strömgren sphere radius. Although 3MDB contains results of partial cuts of radiation bounded models, only fully radiation bounded results (H_β depth >95%) are used.
2. CALIFA has a smaller step size in ionization parameter U than BOND, but covers a slightly smaller range. logU = −4 to −1.5 with a step size = 0.5 is used for both grids.
3. BOND only runs on input SEDs with starburst ages from 1 to 6 Myr with a step size of 1 Myr, while the CALIFA SEDs range from 1 Myr to 14 Gyr, with a more coarse sampling. Ages of 1, 3, 4, and 6 Myr are used in BOND, and 1, 3, 4, and 5.6 Myr are used in CALIFA in the comparison.
4. BOND is run on a wider range in log O/H, but only models with log O/H = −3.2, −3.4, −3.8, and −4.0 are used to overlap with the CALIFA range of log O/H = −3.09, −3.31, −3.71, and −4.02.
5. Again, only BOND models with log N/O = −1.25, −1.0, −0.75, −0.5, and −0.25 are used because CALIFA only has log N/O = −1.36, −1.11, −0.86, −0.61, and −0.36.

These selection cuts result in 480 models in each project, and a combined model count of 960. These photoionization models cover the most commonly discussed parameter space in metallicity, the N/O, and the ionization parameter, so that they form a representative collection for calibrating and diagnosing chemical abundance. It also samples the relatively low metallicities and young stellar populations that are relevant to the dwarf galaxies and LIRGs tested in this paper, and they are usesful for the prospective application to high-redshift counterparts.

3.3. N3O3 Calibrated by Photoionization Models

The N3O3 parameter divided by the N/O of each photoionization model is computed and plotted against the neon-line ratio in the upper left panel in Figure 1. BOND data points are marked by squares and CALIFA data by circles. All the N3O3 are divided and color-coded by the N/O in the models to better illustrate that most of the residual dispersion is due to factors other than the abundance ratio. Only data points with log [Ne III]/[Ne II] between −2 and 2 are shown in the figure, which reflects the dynamical range of currently available spectral observations. As a result, only 820 out of 960 models are shown in the figure. The mean and standard deviation are calculated in bins of size Δ (log [Ne III]/[Ne II]) = 0.5, plotted with the solid black lines and enveloping gray shades. The standard deviation in each bin is interpreted as the error of this diagnostic. As the [Ne III]/[Ne II] increases along the *x*-axis, log *N3O3* gradually converges and flattens to 0, the expected value, but it diverges below 0 at higher neon ratios. This behavior is consistent with the discussion of soft and very hard radiation fields at the beginning of Section 3.1. It shows that the original N3O3 ratio works reasonably well in the regime −0.5 < log [Ne III]/[Ne II] < 1.5, and can be calibrated to function in a wider range of radiation fields with the help of neon-line ratio.

The data points are color-coded by the N/O, and many points that show a continuous gradient of N/O often cluster very closely. This indicates that the N/O has a negligible effect on ionizing structure and emissivity, and the scatter seen in the left figure is mainly due to differences in electron density, metallicity, and radiation strength and is not due to changes in the N/O. This relation is split into abundance groups in the right panels by multiplying with the N/O abundance ratio ranging from log N/O = 0 to −2. This illustrates how the N/O can be determined with the N3O3 to neon-line ratio diagram.

[7] https://sites.google.com/site/mexicanmillionmodels/

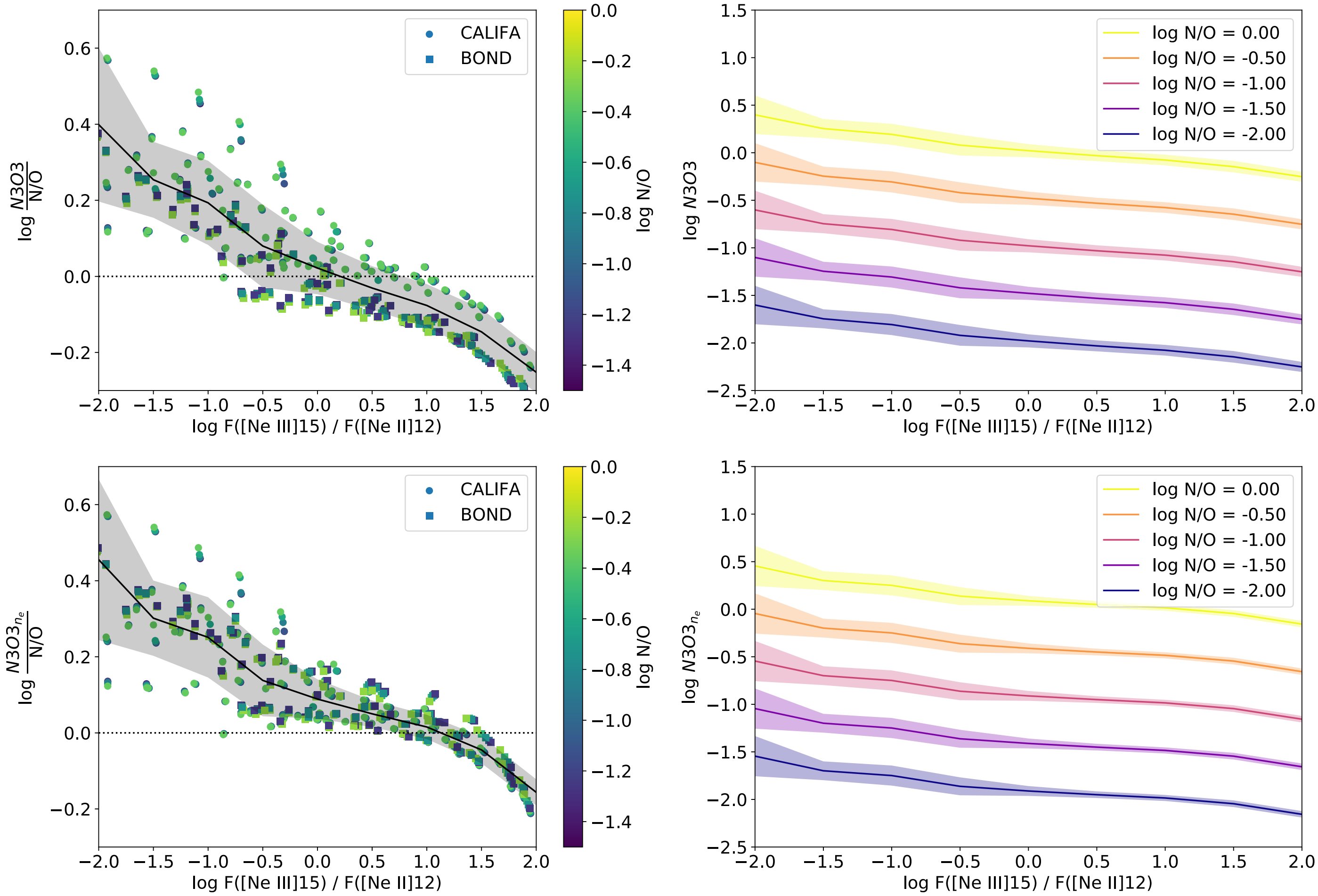

Figure 1. N3O3 (upper panel) and density-corrected N3O3$_{n_e}$(lower panel) parameter of selected photoionization models as a function of the [Ne III]15/[Ne II]12. Shown on the left are N3O3 and N3O3$_{n_e}$ divided by N/O in order to show the intrinsic scatter of the calibration; the right panels show the normalized N3O3 and N3O3$_{n_e}$ vs. neon-line ratio relation as a function of N/O, readily to be applied to estimate the N/O. The shades show the standard deviation in each $\Delta x = 0.5$ bin, which is interpreted as the uncertainty of the relation.

One obvious issue with the upper left panel is that the BOND data points settle below CALIFA by about 0.1 dex, especially in the high [Ne III]/[Ne II] region where N3O3 has the highest accuracy. This is because BOND is run on electron density $n_e = 100\,\mathrm{cm}^{-3}$, resulting in a lower $\varepsilon_{[\mathrm{N\,III}]}/\varepsilon_{[\mathrm{O\,III}]52}$.

The calibration using photoionization models validates the effectiveness of N3O3, as well as a more precise and reliable relation with an error estimation created with the addition of the neon-line-based radiation hardness tracer. However, this calibration also displays some limitations: the N3O3 diagnostic works best in hard radiation environments (log [Ne III]/[Ne II] r > -0.5) because in this regime the N^{++} and O^{++} ionization zones are exactly cospatial; the ratio of N3O3 to the neon-line still has a dispersion of at least 0.03 dex, which largely comes from small variations in the ionization structure that are caused by metallicity differences; and the models used for calibration only cover a limited and sparse sample in large parameter space.

4. Application to a Galaxy Sample

4.1. Galaxy Sample

To demonstrate this new diagnostic, several starburst and low-metallicity galaxies in the local universe are selected for application. The choice is primarily subject to data and observation scheduling availability, but also various factors including the representativeness of the galaxies and their similarity to the supposedly low-metallicity high-redshift galaxies. The galaxy sample and their basic properties are summarized in Table 2.

Arp 299 is an interacting system comprising two galaxies. The nuclear regions of the galaxies are called A (eastern component) and B (southwestern component), separated by about 20″. Component C, located at ∼10″ north of B, is part of the overlapping/external star-forming region (see Neff et al. 2004). Source A is the brightest IR continuum source in the system and hosts a young starburst estimated to have peaked 6–8 Myr ago (Alonso-Herrero et al. 2000). B is the second brightest in the far-IR continuum, but interestingly, the [O III] line coming from B is significantly weaker than its close neighbor C. While C shows the opposite feature, its [O III] emission is almost as bright as A, but the continuum flux density is an order of magnitude lower than B. Because B and C are only separated by ∼10 arcsec and both appear extended, they are blended in both SOFIA/FIFI-LS and Herschel observations, thus they are treated as one source “B&C” in the rest of the paper. Most of the line emission comes from component C, however. Both A and B&C are observed in our SOFIA/FIFI-LS mapping. It is in the Great Observatories All-Sky LIRG Survey (GOALS; Armus et al. 2009) sample as well.

Haro 3 is a blue compact dwarf galaxy (BCD) with two very young starburst regions. One of the two regions hosts a

Table 2
Characteristics of Galaxy Sample

Galaxy name	Type	Redshift
Arp 299	Interacting LIRG	0.010300
Haro 3	BCD	0.003149
II Zw 40	BCD	0.002632
M 83	Spiral	0.001711
MCG+12-02-001	LIRG	0.015698
NGC 2146	LIRG	0.002979
NGC 4194	LIRG	0.008342
NGC 4214	BCD	0.000970

Note. The columns are the common name used in the paper; morphological or luminosity types; galaxy redshift. The type information is from NED(NASA/IPAC Extragalactic Database), Cormier et al. (2015) and Armus et al. (2009); redshifts are taken from NED.

Table 3
Table of SOFIA/FIFI-LS Observations

Target	Line	Obs-ID	T_{exp} [s]
Arp 299	[O III]52	P_2017-02-28_FI_F379B200754	2949.12
Haro 3	[O III]52	P_2018-11-07_FI_F525B01652	1413.12
II Zw 40	[O III]52	P_2018-11-06_FI_F524B01631	768.00
II Zw 40	[N III]	P_2018-11-06_FI_F524B01731	1536.00
M83 nucleus	[O III]52	P_2019-05-04_FI_F565B400205	2119.68
MCG+12-02-001	[O III]52	P_2019-05-01_FI_F562B100373	1320.96
MCG+12-02-001	[N III]	P_2019-05-01_FI_F562B100464	1351.68
NGC 4194	[O III]52	P_2019-05-09_FI_F568B00338	430.08
NGC 4194	[N III]	P_2019-05-09_FI_F568B00366	860.16
NGC 4214 region I	[O III]52	P_2019-02-28_FI_F549B200462	1320.96
NGC 4214 region I	[N III]	P_2019-05-08_FI_F567B00512	1413.12

Note. The columns are the target of the field, the observed far-IR line, the associated SOFIA observation ID, and the exposure time in seconds.

starburst younger than 5 Myr, and the other is $8 \sim 10$ Myr old (Johnson et al. 2004). The stellar mass in Haro 3 is $\sim 10^6\,M_\odot$, and the SFR $\sim 0.8\,M_\odot\,yr^{-1}$ measured by combining far-UV and mid-IR photometry (De Looze et al. 2014). It is included in the Herschel Dwarf Galaxy Survey sample (DGS; Cormier et al. 2015).

II Zw 40 is also a BCD galaxy with a young starburst. The stellar mass is estimated to be $\sim 9 \times 10^5\,M_\odot$, and the SFR $\sim 0.8\,M_\odot yr^{-1}$ (De Looze et al. 2014). The age of the starburst is estimated to be $\sim$3 Myr (Leitherer et al. 2018). II Zw 40 is also in the DGS sample.

MCG+12-02-001 is a LIRG and an interacting system. The stellar mass is about $8 \times 10^{10}\,M_\odot$ and the SFR is 30 to 55 $M_\odot yr^{-1}$ (De Looze et al. 2014; Howell et al. 2010). The starburst age is found to be 40-200 Myr from SED fitting (Pereira-Santaella et al. 2015). It is in the GOALS sample, but this source has very little available optical observational data.

NGC 2146 is a barred spiral galaxy, and it is one of the nearest LIRGs. The SFR is estimated to be 7.9 $M_\odot yr^{-1}$, dominated by the nuclear starburst. It is in the GOALS sample. NGC 2146 has an Infrared Space Observatory (ISO) detection of the [N III] line as well as both of the [O III] lines. In addition, it is the only source that is not classified as "extended" in Brauher et al. (2008) with all three lines detected, and it also has ample optical and mid-IR data available to aide our N/O measurement. While the star formation activities in NGC 2146 are extended over 2′ scales (Stacey et al. 1991), the ISO beam is uniform at about 70″ for these lines and therefore provides good measurements of the inner 4.9 kpc region of this galaxy.

NGC 4194 is a LIRG and a minor merger. Estimates for its SFR disagree, with SFRs ranging from $\sim 46\,M_\odot\,yr^{-1}$ by H_α observation (Hancock et al. 2006) to $\sim 13\,M_\odot\,yr^{-1}$ in the far-IR (De Looze et al. 2014). Most of the star formation occurs in the super star clusters that are thought to be 5 to 15 Myr old (Konig et al. 2014; Pellerin & Robert 2007). It is in the GOALS samples.

NGC 4214 is a BCD galaxy with two main components: region I is the larger component centered on the nucleus and is brighter in the far-IR; region II is a smaller source located about 30 arcsecond to the southeast. Because only region I is within the field of view in our SOFIA/FIFI-LS observations, the discussion in this paper focuses on this component. The SFR in NGC 4214 as a whole is 0.063 $M_\odot\,yr^{-1}$ (De Looze et al. 2014). Its stellar population age is estimated at only 4 to 5 Myr through far-UV photometry (Pellerin & Robert 2007) and UV point-source observations (Williams et al. 2011). It is in the DGS sample.

M83 is a nearby spiral galaxy with a prominent bar. Only the central regions are currently mapped in the [O III] 52 μm line by SOFIA/FIFI-LS, so only the nuclear region of M83 is discussed here. M83 hosts a circumnuclear starburst, which displays a burst age gradient along the star-forming arc spanning from 6 to 8 Myr (Houghton & Thatte 2008; Knapen et al. 2010).

4.2. SOFIA/FIFI-LS Data

One major limitation of the application of the far-IR diagnostics we advocate here is the limited availability of the [O III]52 and [N III] line measurements. During its lifetime, the Herschel Space Observatory (Pilbratt et al. 2010) provided far-IR spectroscopy at unprecedented sensitivity and spatial resolution. However, the 52 μm [O III] line is outside the 55 to 210 μm spectral range of PACS (Poglitsch et al. 2010) for $z < 0.06$ objects. Furthermore, the [N III] line, which is typically about five times weaker than the [O III] line, was not often observed so that Herschel measurements of both the [O III]52 and [N III] lines are very rare. Herschel was decommissioned in 2013. The NASA SOFIA observatory (Temi et al. 2018) fortunately is in operation and can provide the spectroscopy we need for the science presented here.

FIFI-LS (Fischer et al. 2018) is a far-IR IFU onboard SOFIA, with a design and capabilities similar to those of the Herschel/PACS instrument, but with a shorter spectral wavelength cutoff. In the 51–125 μm "blue channel," it has 5×5 spatial pixels (spaxels) of size 6″/pixel. Observations are dithered, so that our maps have finer spatial sampling. The velocity resolution is about 300 km s^{-1} at 50–60 μm.

We obtained new far-IR spectroscopic observations for all of our sources except for NGC 2146 in the period from 2017 February to 2019 May using FIFI-LS on SOFIA. The newly acquired spectral observations are listed in Table 3. All the SOFIA data have gone through level 4 pipeline reduction, which is chopped and corrected for atmospheric transmission. However, for NGC 4214 and MCG+12-02-001, the atmospheric transmission around the [N III] line is problematic, and to produce the [N III] spectra, we manually corrected the raw data for the atmosphere transmission using the information in the spectral cube. This reduction shows a line flux similar to the pipeline reduction, but with a better line shape and improved

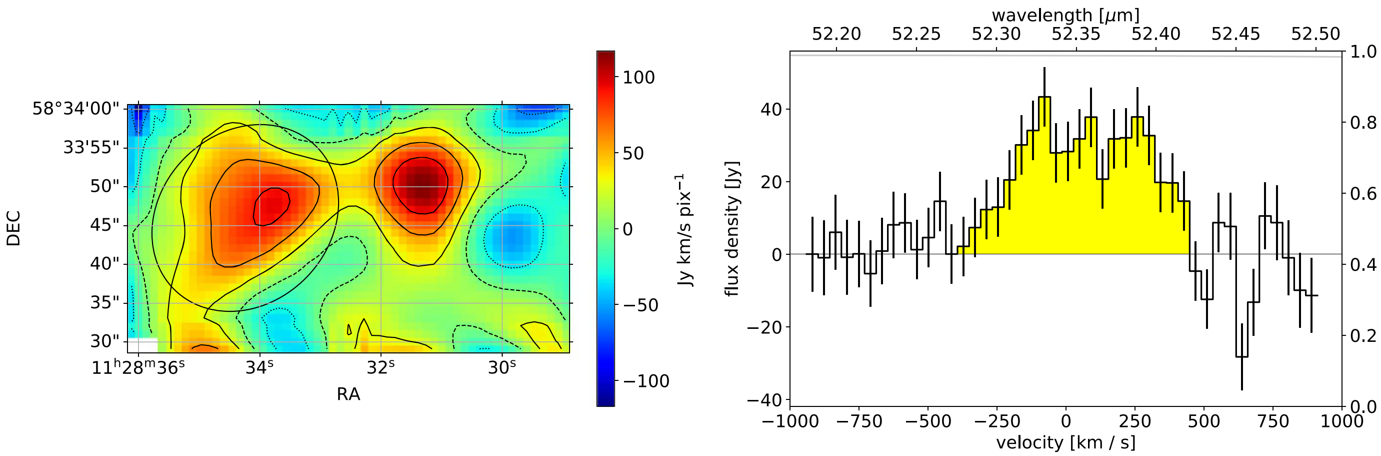

Figure 2. Arp 299 A [O III]52 line map and spectrum. In the left panel, an ellipse is shown representing the region over which the spectrum is measured, and the pixels are color coded by the flux intensity shown in the color bar. The solid contours correspond to +3, +6, +9, etc. times the median of error per pixel in the field. The dashed line labels 0 flux, and dotted lines are −3, −6 the median error levels. In the right panel, the spectrum and one-sigma error is plotted as the solid black line, with the raw atmospheric transmission at the time of observation and that smoothed to the FIFI-LS spectral resolution presented as dotted and solid gray lines. The channels that are integrated to make the line flux map and to measure the line flux are shown in yellow. The complete figure set (11 images) is available in the online journal.

(The complete figure set (11 images) is available.)

signal-to-noise ratio (S/N). For other data sets that were pipeline processed, we also manually restored data channels that were blanked out by the pipeline because the FIFI-LS pipeline blanks channels with transmission < 0.6. We find that this places too harsh a standard on accepting data, and restoring the blanked channels can improve the baseline determination.

The SOFIA/FIFI-LS data are delivered as spectral cubes, and the process of measuring the spectra is as follows: first, the raw data are manually corrected for transmission to fill in the missing channels in the pipeline-corrected data; second, weights (w) are calculated as $w = \mathrm{N} \times \tau$ for each spaxel, where N is the number of scans in each observation and τ is the transmission. The error is calculated based on the rms in spectral dimension, taking into account that $\sigma \propto 1/\sqrt{w}$. The continuum map is then computed at each spatial position as the weighted average of the channels free of the spectral line. The continuum map is later subtracted from the whole spectral cube to produce a continuum-subtracted cube, which is collapsed in spectral dimension to produce a line moment 0 map. Now an ellipse is defined as the emitting region of the spectral line, and integrated in each channel to derive the spectrum. The error estimation takes into account that the noise is correlated across the 5."5 beam. Finally, the line channels in the spectrum are summed as the line flux measurement.

The integrated line flux map and continuum-subtracted spectra for all but NGC 4194 [N III] data are presented in Appendix B and the corresponding figure set, with an example shown in Figure 2. We also plot an ellipse in each line map that shows the region from which the spectrum is extracted. The NGC 4194 [N III] observation is not used in this paper because it lies immediately beside a deep and wide telluric feature, and another narrow feature is at $+200$ km s^{-1} with respect to the expected source line center. The ISO [N III] flux is used instead.

There are several caveats on the spectra. Instead of matching the same areas across different lines, we choose to pick the integration region such that it encloses most of the emission. This is justified by two reasons: first, it would give us the highest S/N for our flux measurement, which is essential for [N III] observations that in some cases only have tentative detections; second, the Herschel/PACS line fluxes used in this work are mostly integrated over a 5 by 5 map, so maximizing the flux in SOFIA/FIFI-LS observation ensures that we include any extended emission contained in the PACS data. This strategy works well when we compare the SOFIA-extracted fluxes with available ISO observations, which have an even larger beam so that it could include more extended emission, and find they agree within 1σ error. Other SOFIA data, especially the [N III] observations, also suffer from the low and/or highly variable transmission. In addition, many spectra have excess noise and sometimes systematic trends in their long- and/or short-wavelength edge channels. This is because FIFI-LS can saturate and enter a nonlinear regime when the foreground (sky + telescope) emission is too strong, and the integration times in the edge channels are far shorter than those in the central channels as the instantaneous FIFI-LS bandwidth is swept across the line to increase spectral coverage (private communication with the SOFIA help desk). These effects complicate baseline determination. The [N III] line from II Zw 40 is also very close to a deep absorption feature. Its baseline turns downward at $v_{\mathrm{rest}} > 150$ km s^{-1} and the error rapidly increases as the telluric transmission declines, making the absolute line flux measurement unreliable. Although the line channels add up to flux $= 5.51 \pm 1.76 \times 10^{-16}$ W m^{-2}, the asymmetric line shape indicates that up to 30% of the flux could be missing. Thus we assess that the uncertainty of the measurement should be 4×10^{-16} W m^{-2}, which is used in the paper.

4.3. Ancillary Data

Herschel/PACS (Poglitsch et al. 2010) provides the largest archive of [N III] and [O III] spectral observations to date. For the sample galaxies, all but NGC 4194 and MCG+12-02-001 have [N III] spectra taken by PACS. Most of the data used here have been processed in Cormier et al. (2015) and Fernández-Ontiveros et al. (2016). Because PACS has a similar field of view as our FIFI-LS maps, the flux measurements by FIFI-LS

Table 4
The Flux of the [N III], [O III]52, [O III]88, [Ne II]12, and [Ne III]15 Lines Used to Obtain the N/O Abuncance

Galaxy name	[N III]	[O III]52	[O III]88	[Ne II]12	[Ne III]15
Arp 299 A	7.3 ± 0.5[a]	40.0 ± 4.28	28 ± 0.32[a]	23.7 ± 0.26[b]	5.70 ± 0.098[b]
Arp 299 B&C	7.2 ± 0.13[a]	30.8 ± 3.72	30 ± 0.26[a]	10.4 ± 0.27[b]	5.44 ± 0.098[b]
Haro 3	1.23 ± 0.17[c]	26.9 ± 2.99	18.4 ± 0.4[c]	3.52 ± 0.13[c]	9.84 ± 0.74[c]
II-Zw 40	5.51 ± 4	48.6 ± 4.52	35.9 ± 0.4[c]	0.735 ± 0.079[c]	14.1 ± 0.9[c]
M83 nucleus	16.6 ± 1.03[d]	22.7 ± 3.03	21.7 ± 0.70[d]	50.3 ± 1.98[d]	2.93 ± 0.077[d]
MCG+12-02-001	5.29 ± 1.53	30.5 ± 3.09	23.4 ± 2.4[e]	20.1 ± 0.21[b]	3.7 ± 0.067[b]
NGC 2146	55.1 ± 5.9[e]	151.4 ± 20.1[e]	157.7 ± 6.5[e]	68.2 ± 0.80[b]	9.81 ± 0.123[b]
NGC 4194	6.5 ± 2.2[e]	31.5 ± 2.8	20.6 ± 1.4[e]	17.57 ± 0.14[b]	5.62 ± 0.06[b]
NGC 4214 region I	1.96 ± 0.70	17.5 ± 1.31	31.9 ± 0.62[f]	8.98 ± 0.22[f]	18.7 ± 0.14[f]

Notes. The unit of the flux is 10^{-16}W m^{-2}.
The line fluxes without superscripts are the SOFIA/FIFI-LS data presented in this work, while the superscripts correspond to the references
[a] J. Hodis et al. 2020, in preparation
[b] Inami et al. (2013);
[c] Cormier et al. (2015);
[d] Fernández-Ontiveros et al. (2016);
[e] Brauher et al. (2008);
[f] Dimaratos et al. (2015).

secure any loss of extended emission compared with that of PACS.

The Infrared Space Observatory (Kessler et al. 1996) supplies the vital far-IR data for MCG+12-02-001, NGC 2146, and NGC 4194. The data were obtained with the ISO/LWS (Clegg et al. 1996) and are spatially unresolved. The line fluxes are taken from Brauher et al. (2008), and the explanation of data reduction details can be found in that paper.

The mid-IR [Ne II] 12.8 μm and [Ne III] 15.5 μm lines are originally observed with Spitzer/IRS in high-resolution mode (Houck et al. 2004; Werner et al. 2004). The flux data are directly taken from Inami et al. (2013) and Cormier et al. (2015), where a description of data processing can be found.

Arp 299 and NGC 4214 are two exceptions as they contain multiple components. The far-IR data of Arp 299 are from Hodis et al. (J. Hodis et al. 2020, in preparation) where fluxes are measured for the A and B&C components separately within a Herschel/PACS map. For NGC 4214, we use both the far-IR and the mid-IR line flux values reported in Dimaratos et al. (2015), who measured two regions individually.

In addition to the neon lines used for calibration, all sources except NGC 4214 have [Ne V] 14.3 μm flux upper limits reported in the same references. The upper limits are at least one order of magnitude lower than their [Ne III] 15.5 μm fluxes, indicating negligible AGN contribution. For NGC 4214, the resolved photometric study in Williams et al. (2011) and photodissociation region (PDR) modeling in Dimaratos et al. (2015) show that the central region is dominated by starburst activity with no trace of AGN. Thus all the sources in our sample have little to no AGN contamination in their [Ne III]15 and [Ne II]12 line fluxes, and the photoionization model calibration based on stellar population synthesis is applicable to this sample.

All the data we use in our application of the N3O3 diagnostic are summarized in Table 4.

4.4. Results

The N3O3 parameter is calculated for each galaxy and then corrected for density by using the [O III]52/88 line ratio to obtain N3O3$_{n_e}$. With these strong line parameters in hand, we computed the [Ne III]15/[Ne II]12 line ratio, and compared it with the calibrated diagnostic as in Section 3.3 to derive the high-precision N/O abundance ratio. The original and density-corrected N3O3 parameters are plotted against our model calibration in Figure 2. Their positions in the diagram represent the N/O estimates. The values of strong line parameters and the calibrated N/O are listed in Table 5.

The derived N/O covers a large range from −1.6 to −0.5 in Table 5. The N/O of different types of galaxies also cluster together: those of dwarf galaxies are systematically lower than those of LIRGs, and the M83 nucleus has the highest value. This is consistent with our understanding of the N/O evolution along with the starburst age and metallicity. The errors also change in an increasing trend as more spectral lines are used and more statistical uncertainty is introduced, but the systematic uncertainty in the calibration would decrease. But the final error budget is often dominated by the [O III]52 and [N III]57 line flux errors.

Note that when the noise is dominated by these two lines, the strong line methods are good estimations of the N/O abundance ratio. Comparing the N3O3 in Column (2), the most simplistic estimation of N/O using only two spectral lines, to the value in Column (5), which is the most precise and reliable diagnostic using five lines, the value changes by <0.15 dex for all targets except for Haro 3 and II Zw 40. This small change arises because the effect of the density correction, which would increase the N/O result, is offset by the model calibration for the log [Ne III]/[Ne II] in the −0.5 to 1.5 range, which would decrease the N/O estimate. For the exceptions Haro 3 and II Zw 40, they have moderately high electron densities as well as hard ionization conditions, resulting in noticeable differences between N3O3 and the model calibration, but the N3O3$_{n_e}$ parameter instead shows great agreement with the model-calibrated results. This indicates that the N3O3 parameter is a good estimator for the N/O abundance when the availability of data is limited, or when the uncertainty is dominated by observational error instead of the intrinsic dispersion of diagnostic, like in the case of samples used here. For galaxies with moderately high electron density and a hard radiation field, such as some dwarf galaxies and high-redshift galaxies, however, N3O3$_{n_e}$ could yield a better N/O estimate than N3O3.

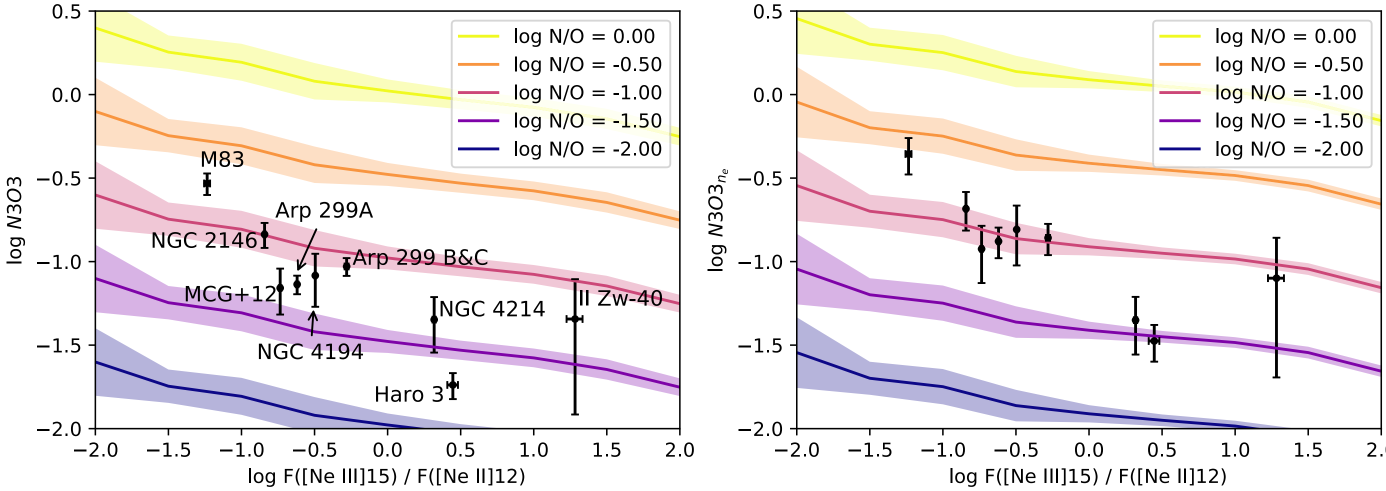

Figure 3. The original and density-corrected N3O3 of the sample galaxies are plotted in the left and right panels, respectively, with model calibration lines of N3O3 and N3O3$_{n_e}$ shown in the background and color-coded by N/O = −2.0 to 0. The relative position between data point and calibrated diagnostic lines indicates the N/O of each galaxy. Each data point is labeled with its name in the left panels, which can be mapped to the right panel by its position on the *x*-axis.

Table 5
N/O Derived Through the N3O3 Strong Line Methods and Model Calibrations

Galaxy Name	Strong Line Method		Model Calibration		log [Ne III]/[Ne II]
	log $N3O3$	log $N3O3_{n_e}$	log N/O by N3O3	log N/O by N3O3$_{n_e}$	
(1)	(2)	(3)	(4)	(5)	(6)
Arp 299 A	$-1.14^{+0.052}_{-0.059}$	$-0.88^{+0.082}_{-0.101}$	$-1.24^{+0.119}_{-0.164}$	$-1.04^{+0.122}_{-0.171}$	−0.62
Arp 299 B&C	$-1.03^{+0.050}_{-0.057}$	$-0.86^{+0.083}_{-0.103}$	$-1.08^{+0.102}_{-0.133}$	$-0.97^{+0.109}_{-0.145}$	−0.28
Haro 3	$-1.74^{+0.071}_{-0.085}$	$-1.48^{+0.096}_{-0.124}$	$-1.71^{+0.089}_{-0.113}$	$-1.53^{+0.101}_{-0.133}$	0.45
II Zw 40	$-1.34^{+0.239}_{-0.572}$	$-1.10^{+0.242}_{-0.594}$	$-1.23^{+0.242}_{-0.595}$	$-1.08^{+0.243}_{-0.602}$	1.28
M83 nucleus	$-0.53^{+0.060}_{-0.069}$	$-0.36^{+0.096}_{-0.123}$	$-0.75^{+0.118}_{-0.163}$	$-0.63^{+0.134}_{-0.195}$	−1.23
MCG+12-02-001	$-1.16^{+0.116}_{-0.159}$	$-0.92^{+0.138}_{-0.204}$	$-1.29^{+0.152}_{-0.237}$	$-1.12^{+0.163}_{-0.264}$	−0.73
NGC 2146	$-0.84^{+0.068}_{-0.081}$	$-0.68^{+0.100}_{-0.131}$	$-0.99^{+0.126}_{-0.177}$	$-0.90^{+0.137}_{-0.201}$	−0.84
NGC 4194	$-1.08^{+0.130}_{-0.187}$	$-0.81^{+0.143}_{-0.215}$	$-1.16^{+0.162}_{-0.261}$	$-0.95^{+0.164}_{-0.267}$	−0.49
NGC 4214 region I	$-1.35^{+0.135}_{-0.197}$	$-1.35^{+0.139}_{-0.206}$	$-1.34^{+0.145}_{-0.219}$	$-1.41^{+0.143}_{-0.215}$	0.32

Note. Columns are (1) name of galaxy as in Table 2; (2) N3O3 parameter calculated for each galaxy; (3) density-corrected N3O3$_{n_e}$ parameter; (4) N/O derived from N3O3 parameter photoionization model calibration, as in the left panel of Figure 3; (5) N/O from density-corrected N3O3$_{n_e}$ parameter as in the right panel of Figure 3; (6) [Ne III]15/[Ne II]12 line flux ratio used for model calibration.

However, using multiple lines and model calibration is still advantageous as it can mitigate the effects of density or radiation hardness in a way that is physically sound. The statistical errors may increase when more lines are used, but systematic errors will decrease, so that the values obtained with the density and radiation field correcting lines are more reliable. Therefore the diagnostic method using more spectral lines is always recommended.

4.5. Comparison with Optical Diagnostics

Of the nine sources that we showed here, only six have optical-line-based N/O abundance measurements in the literature. Haro 3, II Zw 40, and NGC 4214 are in the DGS paper (Cormier et al. 2019), while the NGC 4214 N/O measurement is quoted from Kobulnicky & Skillman (1996) based on the [N II]λ6584/[O II]λ3727 strong line ratio at various positions in long-slit observations. In addition, Kobulnicky & Skillman (1996) also calculated N/O for II Zw 40. Haro 3, M83, NGC 2146, and NGC 4214 are measured in De Vis et al. (2019) using a new calibration in Pilyugin & Grebel (2016), denoted PG16 hereafter. To obtain a global abundance ratio, De Vis et al. (2019) combined observations of various scales including fiber, IFU, and drift scan, then tried to model the N/O gradient and used the value at R_{25}.

One main concern for comparing optical and far-IR N/O measurements is that the optical observations often resolve galaxies and potentially probe smaller regions than the far-IR lines, which use the integrated fluxes of the whole galaxy and measure N/O averaged over a larger aperture. Hence we calculate N/O using the integrated optical spectroscopic observation in Moustakas & Kennicutt (2006), and the N2S2 index defined in Pérez-Montero & Contini (2009). This ensures that the optical-line fluxes also cover the whole galaxy, and the [N II]λ6584-to-[S II]λ6717 + 6731 ratio is insensitive to extinction. The values taken from these papers and recalculated with N2S2 are listed in Table 6 along with those derived from the N3O3$_{n_e}$ model calibration as our best optical estimate of N/O. Figure 4 shows a comparison of these estimates.

For NGC 4214, NGC 2146, and the M83 nucleus, the far-IR derived and optical derived N/O abundance ratios agree within the 1σ error. For Arp 299 A and Arp 299 B&C, however, the

Table 6
Comparison of the N/O Abundance Ratio Derived by Optical Methods and that Computed by N3O3$_{n_e}$ to Ne-line Ratio Model Calibration (Column (5) in Table 5)

Galaxy	Optical log N/O	Far-IR log N/O
Arp 299 A	$-0.85^{+0.026}_{-0.028}$[a]	$-1.04^{+0.122}_{-0.171}$
Arp 299 B&C	$-0.71^{+0.026}_{-0.028}$[a]	$-0.97^{+0.109}_{-0.145}$
Haro 3	$-1.13^{+0.031}_{-0.033}$[a], $-1.06^{+0.088}_{-0.107}$[b], -1.29[c], -1.35[d],	$-1.53^{+0.101}_{-0.133}$
II Zw 40	$-1.30^{+0.029}_{-0.031}$[a], -1.44[c], -1.44[d], $-1.052^{+0.059}_{-0.077}$[e]	$-1.08^{+0.243}_{-0.602}$
M83	$-0.63^{+0.028}_{-0.042}$[b]	$-0.63^{+0.134}_{-0.195}$
NGC 2146	$-0.77^{+0.029}_{-0.031}$[a], $-1.06^{+0.049}_{-0.059}$[b]	$-0.90^{+0.137}_{-0.201}$
NGC 4194	$-0.59^{+0.026}_{-0.028}$[a], -0.5[c]	$-0.95^{+0.164}_{-0.267}$
NGC 4214 region I	$-1.30^{+0.029}_{-0.031}$[a], $-1.28^{+0.017}_{-0.018}$[b], -1.30[d,e],	$-1.41^{+0.143}_{-0.215}$

Notes.
The superscripts correspond to
[a] N/O calculated with the N2S2 index, using spectroscopic data from Moustakas & Kennicutt (2006);
[b] N/O reported in De Vis et al. (2019);
[c] Shi et al. (2005);
[d] Cormier et al. (2019);
[e] Kobulnicky & Skillman (1996).

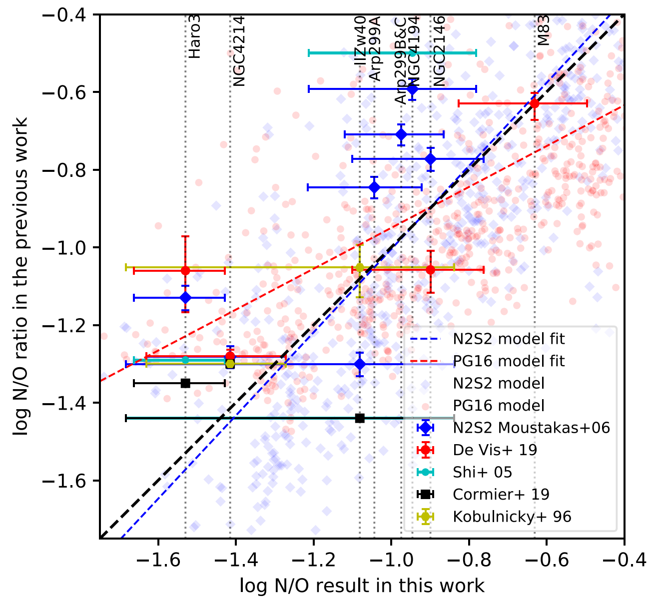

Figure 4. Comparison of the N/O measurement by optical methods to the result of this work. The x-axis is the log N/O diagnosed through density-corrected N3O3$_{n_e}$ index calibrated by neon-line ratio, the y-axis is the N/O measured by optical diagnostics. The opaque data points are plotted as the values listed in Table 6, with different colors and shapes indicating their reference sources. The translucent points are the N/O measurements of photoionization models using N2S2 (blue) and PG16 (red) diagnostics. All the vertical dotted lines correspond to the far-IR N/O results for individual galaxies with their names labeled at the top. The dashed black line shows the one-to-one relation. The blue and red dashed line are the mean least-square fitting to the blue and red translucent points, representing the relation of the photoionization model N/Os measured by the optical N2S2 and PG16 methods against the far-IR method.

optically derived values are 1.5 to 2 σ higher than our N3O3$_{n_e}$ calibrations. In the case of Haro 3 and NGC 4194, there are more than one optical measurement. For Haro 3, the N/Os quoted in Cormier et al. (2015) and Shi et al. (2005) are higher but within $\sim 2\sigma$ away from the one-to-one agreement (diagonal line), while the values in the other two sources are more than 4σ higher than our far-IR result. Similarly, for NGC 4194, the optical results are higher and at 2 to 2.5σ away from the diagonal line. As for II Zw 40, the various optical measurements are off the far-IR estimate but within the 1σ error bar, which is understandable given its highly unreliable measurement of the [N III] flux.

It is worth noting that the optically derived N/Os are overall $\sim$0.2 dex higher than the far-IR results, and N/Os measured by different optical probes do not agree with each other. Therefore we also compare the relation of optical and far-IR N/O diagnostics by computing the N/Os of photoionization models using the optical methods against those by our far-IR approach. The photoionization models are those selected in Section 3.2 for consistency. We adopted two optical measurements, the N2S2 index and PG16, because they are used in our optical N/O calculation and in De Vis et al. (2019), respectively. The optical N/O of models are plotted against far-IR N/O in Figure 4 as blue (N2S2) and red (PG16) translucent points. The model N/Os calculated by N2S2 show a similar trend as the far-IR measurements, and the mean least-square fitting relation (shown as the dashed blue line in Figure 4) suggests a close match between the two methods. However, the N/O estimated by PG16 systematically deviates from the far-IR method and follows a different trend, as shown by the fitted line (dashed red line) in Figure 4. In the figure, PG16 overestimates the N/O in the low N/O regime, then transits to an underestimation for N/O beyond -0.9. This indicates a significant discrepancy of the PG16 calibration with our far-IR method and N2S2. When compared with the fitted lines, the data points of both optical diagnostics show a dispersion of 0.4 dex. Because N2S2 and PG16 are derived through empirical calibration in H II regions, the discrepancy and large scatter seen in the comparison using photoionization models imply systematic differences in the empirical and model-based calibrations. This might be because either the sample of H II regions used for calibrating these diagnostics does not have enough coverage in the physical parameter space, or because the photoionization models explore too large a region in parameter space so that they include physical conditions that are not present in actual galaxies. Calibrations based on individual H II regions could also be at odds with model calibrations that use stellar population synthesis, as the latter is more likely to capture the global properties of a galaxy. Samples of H II regions and photoionization model grids that have finer and wider parameter coverage are required to further study the relationship and reliability of the two types of calibration, but this goes beyond the topic of this work. Even though the N2S2 shows good agreement with the model-calibrated N3O3$_{n_e}$ index, the N/Os of our galaxy sample measured by N2S2 are still distributed in the upper left corner to the fitted line in Figure 4. Hence the difference or the large scatter in the optical to far-IR diagnostics model comparison are not enough to explain the offset in Figure 4.

There are other factors that may affect the result of far-IR N/O estimate and its comparison to optical techniques. The first to consider is the different aperture size for far-IR data. We do not expect a beam effect between SOFIA/FIFI-LS and Herschel/PACS for the reasons stated in Section 4.2. In the case of NGC 4194, ISO [N III] data are used, which have a 75 arcsec aperture and could contain more extended flux than in the SOFIA field.

This would only contribute to <30% of the [N III] flux in ISO data given the small size of NGC 4194, and would lead to an overestimation of N/O instead of an underestimation. As for NGC 2146, it is not affected by aperture size because all the far-IR data are taken from ISO observations. In addition, in order to increase the far-IR N/O estimates by 0.2 dex to match the optical results, it would need either 60% more [N III] flux, or 36% less [O III]52 flux, or the [Ne III]15/[Ne II]12 line ratio to increase by at least tenfold. The beam effect cannot account for such difference. Hence we conclude that the aperture size difference of far-IR data can affect the precision of the line ratio, but does not cause the lower value of N/O that is probed by far-IR lines.

Although the optical N/O results quoted in the previous studies resolve the galaxies, hence they may probe different and much smaller regions than our far-IR measurements, this is not the case for our N2S2 calculation, which uses spectroscopic observations integrated over the whole galaxies. Use of N2S2 also avoids the impact of dust extinction. So the spatial mismatch of regions and extinction may not be responsible for the discrepancy.

However, the optical diagnostics may still probe regions different from the far-IR in terms of physical conditions. Because the optical forbidden lines are enhanced in high-temperature regions while the far-IR fine-structure lines are enhanced in high-density regions, we suspect that the optical lines probe a hotter and more diffuse ISM than the far-IR lines. This means that the optical lines are more susceptible to diffuse ionized gas (DIG). All the optical abundance probes including PG16 and N2S2 rely on the low ionized [N II]λ6584 line, or other low ionized species such as [O II] and [S II] doublets, for which up to 30% of the line emission may arise from DIG. Although the study by Zhang et al. (2017) shows that the [N II]/[S II] is less affected by DIG emission than the indexes using hydrogen recombination lines, we suspect that the N/O measured by N2S2 is still affected by the abundance in DIG that is not probed by the doubly ionized lines used in N3O3. This effect can be non-negligible for massive star-forming galaxies, which host most of the recent star formation activities around the nuclei or in a few compact regions, while the DIG across most of the galaxies is enriched by the relatively old population of stars. It also indicates an interesting approach to study and determine the effect of DIG.

Another factor to consider is that the low and highly ionized lines could come from H II regions with different physical conditions. As optical low ionized lines emerge largely from the population of H II regions that host less massive stars with softer radiation, the ISM probed by the low ionized lines have longer lifetime and could be more enriched with secondary nitrogen. In contrast, far-IR [N III] and [O III] lines are dominated by the dense ISM surrounding young, massive stars with hard radiation fields. These effects combined can also lead to lower N/O probed by highly ionized lines, accounting for the offset shown in the comparison. Detailed chemical evolution models combined with photoionization grids would be needed to test this hypothesis.

We cannot yet draw a conclusion for the cause of the discrepancy in the optical and far-IR derived N/Os. We suggest that this might be related to the systematic differences between the empirical and photoionization model-based calibration, and that optical and far-IR methods probe an ISM of different physical conditions. Both questions touch the fundamental question of the reliability and nature of these abundance diagnostics. To further validate this new N/O diagnostic in nearby galaxies and study the probable difference in optical and far-IR derived N/O, it is essential to obtain more high-quality [O III] 52 μm and [N III]57 μm spectra with SOFIA/FIFI-LS.

5. Summary and Prospective Application to High-z Objects

In this paper, the far-IR [N III]57/[O III]52 line ratio is used to define what we call the N3O3 parameter. We argue that it is a robust way to measure the N/O abundance ratio in galaxies because of the cospatial nature of both ions, and because the emissivity ratio of the lines varies only little. When the [O III] 88 μm line is available, N3O3 can be corrected for the electron density, which is the primary variable affecting the far-IR line ratio. This we call the N3O3$_{n_e}$ parameter. When the [Ne II] 12.8 μm and [Ne III] 15 μm lines are available, this diagnostic can be further improved to cope with the deviations of the diagnostic at soft or very hard radiation fields. Finally, we calibrate the N3O3-to-neon line ratio relation through comparison to photoionization model grids selected from the BOND and CALIFA projects. The model calibration first verifies the tight relation of N3O3 to derive N/O, showing that the residual dispersion for all the models is between 0.05 to 0.1 dex in the range log [Ne III]/[Ne II] between −0.5 and 1.5. It also justifies the need for a density correction, which reduces the dispersion to only 0.03 dex within a certain range of the neon-line ratio. The model calibration in Figure 1 presents the uncertainty of this diagnostics from the standard deviation in small bins along the x-axis, offering a realistic error estimation for the derived N/O values. The model calibration further extends the applicability of N3O3 diagnostics to soft and very hard radiation fields.

The N3O3 diagnostic is applied to a sample of nine sources in eight nearby galaxy systems. All the samples are either BCD or LIRGs and host young starburst components. The results for deriving the N/O using different levels of calibration show that the original N3O3 estimate only differs by ∼0.15 dex for LIRGs when compared with the most precise value output by models that are corrected for both density and ionization effects, while N3O3$_{n_e}$ works better on dwarf galaxies. The increased value of the multiline technique is only achieved for high S/N line detections. In many cases this means that the N3O3 or N3O3$_{n_e}$ parameter is sufficient for abundance determinations.

Only six of our sources have optically derived N/Os in the literature for comparison, so we also calculate N/O by N2S2 index using spectroscopic observations integrated over the whole galaxy, as an attempt to suppress the effect of extinction and spatial mismatch. For three sources our far-IR derived N/Os are in relatively good agreement with the optically derived values. However, for Haro 3, NGC 4194 and both components of Arp 299, the two methods arrive at values that differ by a factor of 1.5 to 2.5, at about 2σ significance. The optical N/O measurements also appear systematically higher than the far-IR results by ∼0.2 dex. To study the relation of different diagnostics, we compared the N/O estimates of photoionization models by those methods. We find that N2S2 agrees well with our model-calibrated N3O3$_{n_e}$ index, while PG16 shows large discrepancy, and both of them have dispersion of 0.4 dex. We point out that there may be a systematic difference in the empirical and model-based calibrations that requires further study.

Although we do not find a definitive explanation for the N/O discrepancy, we can exclude the difference in aperture size, the mismatch of the observed region, and the extinction from causing the offset. We argue it might be linked to the nature of optical low ionized lines and far-IR [N III], [O III] lines, with the former probing hotter regions and suffering from DIG contamination, while the latter gives more weight to dense regions surrounding young, massive stars, leading to measurements of N/O of regions of different physical conditions. This hypothesis requires further study with detailed chemical evolution and photoionization modeling. The large error from the SOFIA/FIFI-LS spectroscopy that is heavily impacted by telluric absorption may also account for part of the difference. To further understand and test this diagnostic, we propose to carry out more observations of [O III] and [N III] lines in nearby galaxies with SOFIA.

Half of the star formation over cosmic time occurs in dusty star-forming galaxies, so the far-IR methods will be important for extinction-free abundance estimates. The high-redshift Universe is also surprisingly dusty, so this is where the N3O3 diagnostic can achieve its full potential. Because it uses just two bright lines that are very close in wavelength, they can both be observed with the ZEUS-2 instrument (Ferkinhoff et al. 2010b), e.g., at selected redshift beyond 2 and will shift into ALMA band 10 at $z \sim 5$. Because the [O III]52 line is one of the brightest far-IR lines, it is relatively easy to detect. This method could also benefit from the growing number of [O III]88 detections at very high redshift (Ferkinhoff et al. 2010a; Inoue et al. 2016; Harikane et al. 2020), as N3O3$_{n_e}$ performs better in the local dwarf galaxies, which are thought to resemble high-z galaxies. Another advantage is that the high-z galaxies are widely conjectured to have radiation fields that are harder than the local star-forming galaxies (Stark 2016; Pavesi et al. 2019; Harikane et al. 2020), pushing the line emission into the regime where the N^{++} and O^{++} species are cospatial in H II regions. This is just the regime where the N/O parameter is least biased and most effective in determining the actual gas-phase N/O abundances. The N/O can help to solve some of the key questions in the early Universe, including how galaxies form and grow through star formation across cosmic time, how the N/O–O/H relation evolves with time, and what the relation between the N/O, metallicity, and gas inflow/outflow is.

We thank the anonymous referee for the insightful feedback that helped us to improve this manuscript. We thank the SOFIA help desk, and in particular, our dedicated support scientist Christian Fisher, for their great help in acquiring and analyzing the SOFIA/FIFI-LS data. Support for this work at Cornell was provided in part by NASA grant NNX17AF37G, NSF grant AST-1716229, NASA/SOFIA grants NAS-97001 (SOF-04-0179, SOF-05-0111), NNA17BF53C (SOF-06-0225, SOF07-0209, SOF08-0165), and the NASA New York Space Grant Consortium. C. Lamarche acknowledges funding support from NASA grant 80NSSC18K0730. C. Ferkinhoff acknowledges support by the National Science Foundation under grant No. 1847892. This work is based on observations made with the NASA/DLR Stratospheric Observatory for Infrared Astronomy (SOFIA). SOFIA is jointly operated by the Universities Space Research Association, Inc. (USRA), under NASA contract NNA17BF53C, and the Deutsches SOFIA Institut (DSI) under DLR contract 50 OK 0901 to the University of Stuttgart. Herschel is an ESA space observatory with science instruments provided by European-led Principal Investigator consortia and with important participation from NASA. The Infrared Space Observatory (ISO) is an European Space Agency (ESA) mission with the participation of ISAS (Japan) and NASA (USA). This Web server is maintained at the ISO Data Centre, which is based at Villafranca, Madrid, and is part of the Science Operations and Data Systems Division of the Research and Scientific Support Department. This work is based in part on archival data obtained with the Spitzer Space Telescope, which was operated by the Jet Propulsion Laboratory, California Institute of Technology under a contract with NASA.

Appendix A
Calculation of N3O3 and the Density Correction

A.1. Basic of Detailed Balancing

The atomic parameters governing collisional excitation and emission of the [N III] and [O III] far-IR fine-structure lines are summarized in Table 7. The collisional strengths between the levels of the ground-state term of O^{++} and N^{++} are taken from Tayal & Zatsarinny (2017) and Blum & Pradhan (1992), both evaluated at $T_e = 10^4$K.

The collisional excitation rate follows the definition in Osterbrock (1989). Here we ignore the electron velocity (temperature) dependence of the rate coefffient. We also assume that the line emission is optically thin: self-absorption and stimulated emission are not important.

A.2. N3O3 at the Low-density Limit

In the low-density limit ($n_e \ll n_{crit}$) approximation, collisional deexcitation is unimportant, and all the ions at the excited states will eventually transit downward by emitting a photon. So only collisional excitation and radiative deexcitation are considered. Because the low-density limit means that radiative transitions are much faster than collisional transitions, to a good approximation, all ions are in the ground state so that the total populations of the ions equals the ground-state population. For the [N III] line in a two-level system, the low-density limit balance is reached when $n_{\rm tot} n_e q_{01} = n_1 A_{10}$, where q_{01} denotes the collisional coefficient from ground state 0 to the first excited state 1. The emissivity is defined here as the power emitted in the specific line per particle per unit time, ignoring the solid angle factor for simplicity. It is calculated as

$$\begin{aligned}\varepsilon_{[\text{N III}],n_e\to 0} &= h\nu_{[\text{N III}]}\,A_{10}\frac{n_1}{n_{\rm tot}}\\ &= 2.161\times 10^{-19}\,\frac{n_e}{T_e^{1/2}}\ \text{erg s}^{-1}. \qquad \text{(A1)}\end{aligned}$$

Table 7
The Collisional and Emission Parameters Used for the Emissivity Calculation of the [N III] and [O III] Emitting Levels

	N III	O III		
Transition	$^2P_{1/2}$, $^2P_{3/2}$	$^3P_0$, $^3P_1$	$^3P_2$, $^3P_1$	$^3P_0$, $^3P_2$
λ(μm)	57.32	88.36	51.81	32.7
$\Omega(i, j)$	1.445	0.542	1.28	0.261
A_{ij}	4.8×10^{-5}	2.6×10^{-5}	9.8×10^{-5}	3.0×10^{-11}

Note. The rows are the transition associated with the line, the line wavelength λ, the collisional strengths $\Omega(i, j)$ between energy level i and j, and the spontaneous emission coefficient $A_{i,j}$.

The calculation for the [O III] 52 μm line follows the same logic, but the balance is between collisional excitation from $^3P_0$ to $^3P_2$, and radiative transitions down from $^3P_2$ to $^3P_1$. Line emission between the $^3P_2$ and $^3P_0$ states is highly forbidden and safely ignored. Therefore the emissivity of the [O III]52 line in the low-density limit is

$$\varepsilon_{[\mathrm{O\,III}]52,n_e\to 0} = 8.635\times 10^{-20}\,\frac{n_e}{T_e^{1/2}}\ \mathrm{erg\ s^{-1}}. \quad \text{(A2)}$$

Then the N3O3 is defined as the line flux ratio divided by the ratio of emissivity,

$$\frac{N}{O} \sim \frac{F([\mathrm{N\,III}])}{F([\mathrm{O\,III}]52)}\,\frac{\varepsilon_{[\mathrm{O\,III}]52,\mathrm{n}_e\to 0}}{\varepsilon_{[\mathrm{N\,III}],n_e\to 0}} = N3O3. \quad \text{(A3)}$$

A.3. N3O3 with $\mathrm{n_e}$ Dependence

To include the density dependence of the line ratios, the balance of collisional excitation or deexcitation and spontaneous radiation from all the levels in the ground-state term must be taken into account. The optically emitting excited terms in the electronic configuration lie high (∼30,000 K) above ground and have high radiative transition probabilities so their level populations will be small compared with those in the ground term. Ignoring these transitions will therefore have negligible effects on the far-IR line emission.

For the N^{++} ion, the detailed balancing is then $n_e n_1 q_{10} + n_1 A_{10} = n_e n_0 q_{01}$ and the emissivity is

$$\varepsilon_{[\mathrm{N\,III}]} = h\nu_{[\mathrm{N\,III}]}\,A_{10}\,\frac{n_e q_{01}}{n_e(q_{01}+q_{10})+A_{10}} = \frac{2.161\times 10^{-19}}{0.1949+\frac{T_e^{1/2}}{n_e}}\ \mathrm{erg\ \ s^{-1}}. \quad \text{(A4)}$$

The calculation for the O^{++} ion is similar but more complicated as it involves three levels. The equations are straightforward to solve (see Osterbrock 1989), and the net result is

$$\varepsilon_{[\mathrm{O\,III}]52} = h\nu_{[\mathrm{O\,III}]52}A_{21}\frac{n_2}{n_{\mathrm{tot}}} = 8.635\,\frac{\frac{n_e}{T_e^{1/2}}\left(1+0.4956\frac{n_e}{T_e^{1/2}}\right)}{1+0.3766\frac{n_e}{T_e^{1/2}}+0.02050\left(\frac{n_e}{T_e^{1/2}}\right)^2}\times 10^{-20}\ \mathrm{erg\ s^{-1}}. \quad \text{(A5)}$$

In the low-density limit, the line emissivity approaches the result calculated in Equations (A1) and (A2). The density-corrected line ratio is then expressed as

$$\frac{N}{O} \sim \frac{F([\mathrm{N\,III}])}{F([\mathrm{O\,III}]52)}\,\frac{\varepsilon_{[\mathrm{O\,III}]52}}{\varepsilon_{[\mathrm{N\,III}]}} = N3O3\times\frac{\left(0.1621+\frac{T_e^{1/2}}{n_e}\right)\frac{n_e}{T_e^{1/2}}\left(1+0.4956\frac{n_e}{T_e^{1/2}}\right)}{1+0.3766\frac{n_e}{T_e^{1/2}}+0.02050\left(\frac{n_e}{T_e^{1/2}}\right)^2} = N3O3_{n_e}. \quad \text{(A6)}$$

When we introduce the temperature dependence $\frac{n_e}{T_e^{1/2}}$ factor in Equation (A6) with the [O III]52/88 line ratio $R_{52/88} = 10.72 - \frac{396.4}{\frac{n_e}{T_e^{1/2}}+39.00}$, we obtain the diagnostic as a function of [O III]52/88 in Equation (4).

ORCID iDs

B. Peng https://orcid.org/0000-0002-1605-0032
C. Lamarche https://orcid.org/0000-0003-1874-7498
A. Vishwas https://orcid.org/0000-0002-4444-8929
C. Ferkinhoff https://orcid.org/0000-0001-6266-0213
C. Rooney https://orcid.org/0000-0002-8513-2971
C. Ball https://orcid.org/0000-0002-1895-0528
D. Brisbin https://orcid.org/0000-0002-4795-419X
J. Higdon https://orcid.org/0000-0003-1397-0586
S. J. U. Higdon https://orcid.org/0000-0002-4021-7453

References

Alonso-Herrero, A., Rieke, G. H., Rieke, M. J., & Scoville, N. Z. 2000, ApJ, 532, 845
Armus, L., Mazzarella, J. M., Evans, A. S., et al. 2009, PASP, 121, 559
Belfiore, F., Maiolino, R., Tremonti, C., et al. 2017, MNRAS, 469, 151
Blum, R. D., & Pradhan, A. K. 1992, ApJS, 80, 425
Brauher, J. R., Dale, D. A., & Helou, G. 2008, ApJS, 178, 280
Cid Fernandes, R., Gónzalez Delgado, R. M., Garcia-Benito, R., et al. 2014, A&A, 561, A130
Clegg, P. E., Ade, P. A. R., Armand, C., et al. 1996, A&A, 315, L38
Contini, M. 2017, MNRAS, 469, 3125
Cormier, D., Madden, S. C., Lebouteiller, V., et al. 2015, A&A, 578, A53
Cormier, D., Abel, N. P., Hony, S., et al. 2019, A&A, 626, A23
Coziol, R., Reyes, R. E. C., Considère, S., Davoust, E., & Contini, T. 1999, A&A, 345, 733
De Looze, I., Cormier, D., Lebouteiller, V., et al. 2014, A&A, 568, A62
De Vis, P., Jones, A., Viaene, S., et al. 2019, A&A, 623, A5
Denicoló, G., Terlevich, R., & Terlevich, E. 2002, MNRAS, 330, 69
Díaz-Santos, T., Armus, L., Charmandaris, V., et al. 2017, ApJ, 846, 32
Dimaratos, A., Cormier, D., Bigiel, F., & Madden, S. C. 2015, A&A, 580, A135
Edmunds, M. G., & Pagel, B. E. J. 1978, MNRAS, 185, 77P
Ferkinhoff, C., Hailey-Dunsheath, S., Nikola, T., et al. 2010a, ApJL, 714, L147
Ferkinhoff, C., Nikola, T., Parshley, S. C., et al. 2010b, Proc. SPIE, 7741, 77410Y
Ferkinhoff, C., Brisbin, D., Nikola, T., et al. 2011, ApJL, 740, L29
Ferland, G. J., Chatzikos, M., Guzmán, F., et al. 2017, RMxAA, 53, 385
Fernández-Ontiveros, J. A., Spinoglio, L., Pereira-Santaella, M., et al. 2016, ApJS, 226, 19
Fischer, C., Beckmann, S., Bryant, A., et al. 2018, JAI, 7, 1840003
Garnett, D. R. 1990, ApJ, 363, 142
Gorjian, V., Cleary, K., Werner, M. W., & Lawrence, C. R. 2007, ApJL, 655, L73
Hancock, M., Weistrop, D., Nelson, C. H., & Kaiser, M. E. 2006, AJ, 131, 282
Harikane, Y., Ouchi, M., Inoue, A. K., et al. 2020, ApJ, 896, 93
Henry, R. B. C., Edmunds, M. G., & Köppen, J. 2000, ApJ, 541, 660
Houck, J. R., Roellig, T. L., van Cleve, J., et al. 2004, ApJS, 154, 18
Houghton, R. C. W., & Thatte, N. 2008, MNRAS, 385, 1110
Howell, J. H., Armus, L., Mazzarella, J. M., et al. 2010, ApJ, 715, 572
Inami, H., Armus, L., Charmandaris, V., et al. 2013, ApJ, 777, 156
Inoue, A. K., Tamura, Y., Matsuo, H., et al. 2016, Sci, 352, 1559
Johnson, K. E., Indebetouw, R., Watson, C., & Kobulnicky, H. A. 2004, AJ, 128, 610
Kessler, M. F., Steinz, J. A., Anderegg, M. E., et al. 1996, A&A, 315, L27
Kewley, L. J., & Dopita, M. A. 2002, ApJS, 142, 35
Knapen, J. H., Sharp, R. G., Ryder, S. D., et al. 2010, MNRAS, 408, 797
Kobulnicky, H. A., & Skillman, E. D. 1996, ApJ, 471, 211
Konig, S., Aalto, S., Lindroos, L., et al. 2014, A&A, 569, A6
Leitherer, C., Byler, N., Lee, J. C., & Levesque, E. M. 2018, ApJ, 865, 55
Lester, D. F., Dinerstein, H. L., Werner, M. W., et al. 1987, ApJ, 320, 573
Lester, D. F., Dinerstein, H. L., Werner, M. W., Watson, D. M., & Genzel, R. L. 1983, ApJ, 271, 618
Mollá, M., Vílchez, J. M., Gavilán, M., & Díaz, A. I. 2006, MNRAS, 372, 1069
Morisset, C. 2013, Astrophysics Source Code Library, ascl:1304.020

Morisset, C., Delgado-Inglada, G., & Flores-Fajardo, N. 2015, RMxAA, 51, 103
Mouhcine, M., & Contini, T. 2002, A&A, 389, 106
Moustakas, J., & Kennicutt, R. C. J. 2006, ApJS, 164, 81
Nagao, T., Maiolino, R., Marconi, A., & Matsuhara, H. 2011, A&A, 526, A149
Neff, S. G., Ulvestad, J. S., & Teng, S. H. 2004, ApJ, 611, 186
Osterbrock, D. E. 1989, Astrophysics of Gaseous Nebulae and Active Galactic Nuclei (Sausalito, CA: University Science Books)
Pagel, B. E. J., Simonson, E. A., Terlevich, R. J., & Edmunds, M. G. 1992, MNRAS, 255, 325
Pavesi, R., Riechers, D. A., Faisst, A. L., Stacey, G. J., & Capak, P. L. 2019, ApJ, 882, 168
Pellerin, A., & Robert, C. 2007, MNRAS, 381, 228
Pereira-Santaella, M., Rigopoulou, D., Farrah, D., Lebouteiller, V., & Li, J. 2017, MNRAS, 470, 1218
Pereira-Santaella, M., Alonso-Herrero, A., Colina, L., et al. 2015, A&A, 577, A78
Pérez-Montero, E., & Contini, T. 2009, MNRAS, 398, 949
Pérez-Montero, E., Contini, T., Lamareille, F., et al. 2013, A&A, 549, A25
Pérez-Montero, E., Garcia-Benito, R., Vílchez, J. M., et al. 2016, A&A, 595, A62
Pettini, M., & Pagel, B. E. J. 2004, MNRAS, 348, L59
Pilbratt, G. L., Riedinger, J. R., Passvogel, T., et al. 2010, A&A, 518, L1
Pilyugin, L. S., & Grebel, E. K. 2016, MNRAS, 457, 3678
Pilyugin, L. S., Thuan, T. X., & Vílchez, J. M. 2003, A&A, 397, 487
Pilyugin, L. S., Vílchez, J. M., & Thuan, T. X. 2010, ApJ, 720, 1738
Poglitsch, A., Waelkens, C., Geis, N., et al. 2010, A&A, 518, L2
Rigopoulou, D., Pereira-Santaella, M., Magdis, G. E., et al. 2018, MNRAS, 473, 20
Rubin, R. H. 1985, ApJS, 57, 349
Rubin, R. H., Simpson, J. P., Erickson, E. F., & Haas, M. R. 1988, ApJ, 327, 377
Sánchez, S. F., Kennicutt, R. C., Gil de Paz, A., et al. 2012, A&A, 538, A8
Schaefer, A. L., Tremonti, C., Belfiore, F., et al. 2020, ApJL, 890, L3
Shi, F., Kong, X., Li, C., & Cheng, F. Z. 2005, A&A, 437, 849
Stacey, G. J. 2011, ITTST, 1, 241
Stacey, G. J., Geis, N., Genzel, R., et al. 1991, ApJ, 373, 423
Stark, D. P. 2016, ARA&A, 54, 761
Stasinska, G. 2019, arXiv:1906.04520
Tayal, S. S., & Zatsarinny, O. 2017, ApJ, 850, 147
Temi, P., Hoffman, D., Ennico, K., & Le, J. 2018, JAI, 7, 1840011
Unger, S. J., Clegg, P. E., Stacey, G. J., et al. 2000, A&A, 355, 885
Vale Asari, N., Stasińska, G., Morisset, C., & Cid Fernandes, R. 2016, MNRAS, 460, 1739
van Zee, L., Salzer, J. J., & Haynes, M. P. 1998, ApJL, 497, L1
Vangioni, E., Dvorkin, I., Olive, K. A., et al. 2018, MNRAS, 477, 56
Viironen, K., Delgado-Inglada, G., Mampaso, A., Magrini, L., & Corradi, R. L. M. 2007, MNRAS, 381, 1719
Vila-Costas, M. B., & Edmunds, M. G. 1993, MNRAS, 265, 199
Vincenzo, F., Belfiore, F., Maiolino, R., Matteucci, F., & Ventura, P. 2016, MNRAS, 458, 3466
Werner, M. W., Roellig, T. L., Low, F. J., et al. 2004, ApJS, 154, 1
Williams, B. F., Dalcanton, J. J., Gilbert, K. M., et al. 2011, ApJ, 735, 22
Zhang, K., Yan, R., Bundy, K., et al. 2017, MNRAS, 466, 3217